GEOPHYSICS, VOL. 86, NO. 4 (JULY-AUGUST 2021); P. R589–R602, 16 FIGS., 1 TABLE.
10.1190/GEO2020-0512.1

Elastic FWI for orthorhombic media with lithologic constraints applied via machine learning

Sagar Singh[1], Ilya Tsvankin[1], and Ehsan Zabihi Naeini[2]

ABSTRACT

Full-waveform inversion (FWI) of 3D wide-azimuth data for elastic orthorhombic media suffers from parameter trade-offs which cannot be overcome without constraining the model-updating procedure. We present an FWI methodology that incorporates geologic constraints to reduce the inversion nonlinearity and increase the resolution of parameter estimation for orthorhombic models. These constraints are obtained from well logs, which can provide rock-physics relationships for different geologic facies. Because the locations of the available well logs are usually sparse, a supervised machine-learning (ML) algorithm (Support Vector Machine) is employed to account for lateral heterogeneity in building the lithologic constraints. The advantages of the facies-based FWI are demonstrated on the modified SEG-EAGE 3D overthrust model, which is made orthorhombic with the symmetry planes that coincide with the Cartesian coordinate planes. We employ a velocity-based parameterization, whose suitability for FWI was studied using the radiation-pattern analysis. Application of the facies-based constraints substantially increases the resolution of the P- and S-wave vertical velocities (V_{P0}, V_{S0}, and V_{S1}) and, therefore, of the depth scale of the model. Improvements are also observed for the P-wave horizontal and normal-moveout velocities (V_{P1}, V_{P2}, $V_{nmo,1}$, and $V_{nmo,2}$) and the S-wave horizontal velocity V_{S2}. However, the velocity $V_{nmo,3}$ that depends on Tsvankin's parameter $\delta^{(3)}$ defined in the horizontal plane is not well recovered from the surface data. On the whole, the developed algorithm achieves a much higher spatial resolution compared to unconstrained FWI, even in the absence of recorded frequencies below 2 Hz.

INTRODUCTION

Elastic full-waveform inversion (Tarantola, 1984) is a promising tool for building high-resolution velocity models and improving the quality of the output from seismic imaging workflows. There has been considerable progress in extending FWI to anisotropic media but the majority of existing studies are limited to transversely isotropic (TI) models with a vertical or tilted symmetry axis (e.g., Kamath and Tsvankin, 2016; Rusmanugroho et al., 2017; Singh et al., 2019, 2020a). Transverse isotropy adequately describes the elastic properties of unfractured shale formations and finely layered sequences in typical sedimentary basins. However, the presence of natural fracture sets and/or nonhydrostatic stresses reduces the medium symmetry to at least orthorhombic (Bakulin et al., 2000; Tsvankin and Grechka, 2011).

There is ample evidence suggesting that orthorhombic symmetry represents the most common type of azimuthal anisotropy in the subsurface (Tsvankin and Grechka, 2011; Tsvankin, 2012; Xie et al., 2017; Maitra et al., 2018; Masmoudi and Alkhalifah, 2018). The large number of independent parameters needed to describe orthorhombic media leads to serious complications in FWI. In particular, parameter trade-offs may cause a substantial deterioration of the inversion results. Therefore, a careful choice of parameterization (e.g., Alkhalifah and Plessix, 2014) is essential in applying FWI to orthorhombic media.

Tsvankin (1997) introduces a widely used notation for orthorhombic models that includes two vertical velocities and seven dimensionless Thomsen-style (Thomsen, 1986) anisotropy coefficients. This notation, based on a limited analogy between the symmetry planes of orthorhombic and TI media, provides a concise description of seismic signatures and facilitates application of velocity-analysis and inversion algorithms to orthorhombic models (Tsvankin, 1997; 2012).

Manuscript received by the Editor 17 July 2020; revised manuscript received 4 January 2021; published ahead of production 11 May 2021; published online 13 July 2021.
[1]Colorado School of Mines, Center for Wave Phenomena, Golden, Colorado 80401, USA. E-mail: sagarsingh@mymail.mines.edu (corresponding author); ilya@mines.edu.
[2]Earth Science Analytics, New Malden, London KT3 5HF, UK. E-mail: ehsanzabihi@yahoo.com.

DOI:10.1190/geo2020-0512.1

Analyzing radiation (scattering) patterns of the medium parameters can yield valuable insights into potential trade-offs and the types of data required for reliable parameter estimation. Oh and Alkhalifah (2016, 2019) study the radiation patterns for different parameterizations of elastic orthorhombic media and conclude that the so-called "deviation parameters" (the differences between the anisotropy coefficients defined in the vertical symmetry planes) can help mitigate the trade-offs in FWI. However, the difference between two typically small anisotropy coefficients may not be a stable quantity in the presence of realistic parameter errors.

Here, we describe the orthorhombic model in terms of the P- and S-wave velocities along the symmetry directions and the P-wave normal-moveout (NMO) velocities. This parameterization inherits the advantages of Tsvankin's notation and represents an extension of the notations proposed by Wang and Tsvankin (2018) for acoustic orthorhombic media and by Kamath and Tsvankin (2016) for elastic VTI media. Singh and Tsvankin (2020) study the radiation patterns of these parameters for an orthorhombic perturbation embedded in a VTI background. The results of their analysis are helpful in properly implementing elastic FWI for orthorhombic media, as discussed below.

The velocity-based parameterization is also convenient for FWI because all parameters have the same units and similar magnitudes, which is also true for the inversion gradients. Additionally, the velocities often have a similar spatial distribution, so a single migrated section can be used to implement image-guided interpolation (see below).

Still, even an optimal parameterization is generally insufficient to eliminate parameter trade-offs in FWI for anisotropic media. Therefore, it is essential to impose constraints on model updating using, for example, prior lithologic information about the subsurface (Zhang et al., 2018; Singh et al., 2018). Zhang and Alkhalifah (2019, 2020) apply a deep neural network (DNN) to constrain the inversion workflow by generating the spatial distribution of prior information represented by geologic facies. They build the initial model by training the network on the parameters obtained by unconstrained FWI with the goal of identifying the relationships between these parameters and borehole data. Singh et al. (2018, 2020b) use image-guided interpolation for TI media to build lithologic constraints that account for lateral heterogeneity. They show that these facies-based constraints can reduce the inversion nonlinearity and increase parameter resolution even for hydrophone (pressure) data. Their inversion algorithm also produces a facies model that could be highly beneficial for reservoir characterization. Here, we extend their approach to orthorhombic media and enhance it by incorporating machine learning.

Initial models for FWI are often obtained from reflection tomography or other post-migration or data-domain velocity-analysis methods. Most anisotropic velocity-inversion techniques are designed for TI media with a vertical or tilted symmetry axis (Grechka and Tsvankin, 1998; Li and Yuan, 1999; Tsvankin and Grechka, 2011; Tsvankin, 2012; Wang and Tsvankin, 2013a, 2013b). Long-wavelength orthorhombic models can be built by applying nonhyperbolic moveout inversion or the inversion of NMO ellipses, also called "stacking-velocity tomography" (Grechka et al., 2005; Vasconcelos and Tsvankin, 2006; Tsvankin and Grechka, 2011; Li et al., 2012; Liu and Tsvankin, 2019). Here, we construct the initial model by performing 2D FWI in the vertical symmetry planes of orthorhombic media.

We begin by describing the FWI methodology for 3D wide-azimuth data from elastic orthorhombic media. Then a modified orthorhombic 3D overthrust model is used to carry out unconstrained inversion of multicomponent surface data. To incorporate lithologic information into FWI, we introduce an efficient technique designed to build facies-based constraints from borehole data using machine learning. Application to the overthrust model demonstrates the benefits of the lithologic constraints in mitigating the inversion nonlinearity and increasing the resolution of most estimated parameters. The machine-learning algorithm incorporated into the FWI framework also generates a high-resolution facies model suitable for reservoir characterization.

ELASTIC FWI FOR ORTHORHOMBIC MEDIA

We employ the l^2-norm objective function to minimize the misfit between the observed ($\mathbf{d}_{\text{obs}}$) and simulated ($\mathbf{d}_{\text{sim}}$) displacement:

$$E(\mathbf{m}) = \sum_{s=1}^{n_s} \|\mathbf{d}_{\text{obs}} - \mathbf{d}_{\text{sim}}(\mathbf{m})\| + \beta \|\mathbf{W}_m(\mathbf{m}_{\text{inv}} - \mathbf{m}_{\text{prior}})\|^2, \tag{1}$$

where $\mathbf{m}$ is the vector of model parameters, n_s is the number of sources, $\mathbf{m}_{\text{inv}}$ and $\mathbf{m}_{\text{prior}}$ are the inverted and prior model, respectively, and $\mathbf{W}_m$ is a weighting matrix. The second term in equation 1 is employed to regularize the objective function, and the scaling coefficient β can be adjusted depending on the reliability of the prior information (Singh et al., 2020b). The vector $\mathbf{d}$ generally includes all three displacement components, and the differences between the observed and simulated data are computed for each component separately.

The large number of independent parameters of orthorhombic media makes the inversion highly nonlinear, often with multiple local minima of the objective function. For such multimodal objective functions, it is essential that the initial model lie in the immediate vicinity (basin of convergence) of the global minimum. Note that the nonuniqueness of the inverse problem can also be caused by the flatness of the objective function near its global minimum.

We simulate the displacement $\mathbf{u}$ for heterogeneous orthorhombic media using the elastic wave equation:

$$\rho \frac{\partial^2 u_i}{\partial t^2} = \frac{\partial}{\partial x_j}\left[c_{ijkl}\frac{\partial u_k}{\partial x_l}\right] + F_i, \tag{2}$$

where ρ is the density, $\mathbf{F}$ is the body force per unit volume, and $c_{ijkl}(i, j, k, l = 1, 2, 3)$ are the stiffness coefficients; summation over repeated indices is implied.

Notation and inversion gradients

We assume that the three orthogonal symmetry planes of orthorhombic media coincide with the Cartesian coordinate planes. Then the model is described by nine generally independent stiffness coefficients and density (Figure 1). Tsvankin (1997, 2012) uses the analogous form of the Christoffel equation in the symmetry planes of orthorhombic and TI media to replace the stiffnesses with the following parameters:

V_{P0}: the P-wave vertical velocity;
V_{S0}: the vertical velocity of the S-wave polarized in the x_1-direction;
$\epsilon^{(1)}$, $\delta^{(1)}$, and $\gamma^{(1)}$: the VTI parameters in the $[x_2, x_3]$-plane (the superscript indicates the axis perpendicular to the corresponding plane);
$\epsilon^{(2)}$, $\delta^{(2)}$, and $\gamma^{(2)}$: the VTI parameters in the $[x_1, x_3]$-plane;
$\delta^{(3)}$: the VTI parameter in the $[x_1, x_2]$-plane (x_1 plays the role of the symmetry axis).

This notation reduces the number of independent parameters responsible for P-wave kinematics from nine to six (V_{P0}, $\epsilon^{(1)}$, $\delta^{(1)}$, $\epsilon^{(2)}$, $\delta^{(2)}$, and $\delta^{(3)}$) and has other important advantages for processing and inversion of seismic data (Tsvankin, 1997, 2012).

Following Kamath and Tsvankin (2016) and Wang and Tsvankin (2018), we parameterize the model in terms of the velocities listed below that represent simple functions of Tsvankin's anisotropy coefficients:

$$V_{P1} = V_{P0}\sqrt{1+2\epsilon^{(1)}}, \tag{3}$$

$$V_{P2} = V_{P0}\sqrt{1+2\epsilon^{(2)}}, \tag{4}$$

$$V_{nmo,1} = V_{P0}\sqrt{1+2\delta^{(1)}}, \tag{5}$$

$$V_{nmo,2} = V_{P0}\sqrt{1+2\delta^{(2)}}, \tag{6}$$

$$V_{nmo,3} = V_{P0}\sqrt{1+2\delta^{(3)}}, \tag{7}$$

$$V_{S1} = V_{S0}\sqrt{\frac{1+2\gamma^{(1)}}{1+2\gamma^{(2)}}}, \tag{8}$$

$$V_{S2} = V_{S0}\sqrt{1+2\gamma^{(1)}}, \tag{9}$$

where V_{P1}, V_{P2}, and V_{P0} are the P-wave velocities in the x_2-, x_1-, and x_3-directions, respectively, $V_{nmo,1}$ and $V_{nmo,2}$ are the P-wave NMO velocities from a horizontal reflector in the $[x_2, x_3]$-, and $[x_1, x_3]$-planes, respectively, $V_{nmo,3}$ is a similarly defined parameter that absorbs the influence of the coefficient $\delta^{(3)}$, $V_{S1} = \sqrt{c_{44}/\rho}$ is the vertical velocity of the S-wave polarized in the x_2-direction, and $V_{S2} = \sqrt{c_{66}/\rho}$ is the horizontal velocity of the SH-waves in both vertical symmetry planes. (Note that these SH-waves represent two different modes, the fast split shear wave S_1 and the slow wave S_2, in the $[x_1, x_3]$- and $[x_2, x_3]$-planes.)

The gradient of the objective function is obtained by differentiating equation 1:

$$\frac{\partial E(\mathbf{m})}{\partial \mathbf{m}} = -\left[\frac{\partial \mathbf{d}_{sim}}{\partial \mathbf{m}}\right]^T [\mathbf{d}_{obs} - \mathbf{d}_{sim}(\mathbf{m})] + \beta\, \mathbf{W}_m^T \mathbf{W}_m (\mathbf{m}_{inv} - \mathbf{m}_{prior}). \tag{10}$$

As in most FWI algorithms, the inversion gradient from equation 10 is computed by the adjoint-state method (e.g., Liu and Tromp, 2006; Kamath and Tsvankin, 2016).

The relationships between the stiffness coefficients and the velocities defined in equations 3–9, as well as the exact expressions for the inversion gradients (for $\beta = 0$) can be found in Appendix A. For the numerical examples below, iterative parameter updating is carried out with a multiscale approach using the nonlinear conjugate-gradient method (e.g., Hager and Zhang, 2006).

The elastic wave equation (equation 2) is solved using a fourth-order (in space) and second-order (in time) finite-difference algorithm on a staggered grid with the convolutional perfectly matched layers (CPML) boundary conditions on the model sides (except for the top, which represents a free surface). To reduce the computational cost associated with handling large-scale elastic 3D models, we apply the domain-decomposition method (Bohlen, 2002).

Synthetic example

We test the developed FWI algorithm on a modified SEG-EAGE 3D overthrust model, which is discretized on a 400 × 400 × 140 grid (Figure 2). To mitigate grid dispersion, the spatial grid spacing dh has to satisfy the following criterion:

$$dh = \frac{V_{min}}{n f_{max}}, \tag{11}$$

where V_{min} is the minimum velocity in the model, f_{max} is the maximum frequency of the source signal, and $n = 8$ for fourth-order finite-different operators. For our model, $V_{min} = 1.82$ km/s and $f_{max} \approx 19$Hz. To completely eliminate dispersion, we set $dh = 10$, which corresponds to a physical domain of 4.0 km × 4.0 km × 1.4 km.

The anisotropy coefficients are obtained by scaling the P- and S-wave velocity fields of the original isotropic model (herein referred to as V_{P0} and V_{S0}), so all parameters have a similar spatial structure. The multicomponent data are recorded with a time increment of

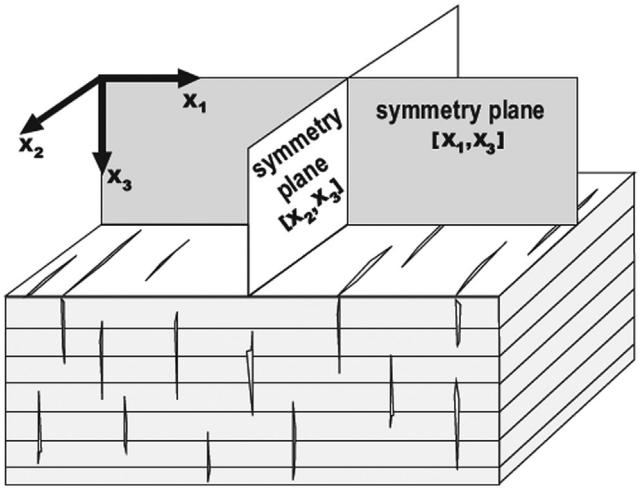

Figure 1. Orthorhombic model formed by parallel vertical fractures embedded in a background VTI medium. One of the symmetry planes is horizontal, and the other two are parallel and perpendicular to the fractures (adapted from Tsvankin, 2012).

0.8 ms at the bottom of the water layer ("sea floor"). The wavefield is excited by 100 shots (point explosions) and recorded by 3600 receivers evenly distributed over a horizontal plane and placed 40 m and 240 m, respectively, beneath the surface. To reduce undesirable reflections from the sides of the model, we employ a 100-m thick CPML boundary (except for the free surface on top). The source signal is a Ricker wavelet with a central frequency of 10 Hz.

Parallelization of the modeling algorithm is based on domain decomposition. The model is separated into subdomains, and the wavefield is updated within each subdomain by the corresponding processing element. We use a Message Passing Interface (2018 Intel MPI) to assign subdomains to different processing elements, which also provides a connection between these distributed domains needed to exchange the values of the updated velocity and stress fields. We use a total of 20 processing elements, so the model is divided into 20 equal subdomains. All three displacement components are inverted simultaneously.

Initial model building

An accurate initial model is essential for FWI, especially when inverting for multiple medium parameters. As mentioned above, we assume that the symmetry planes of the orthorhombic medium coincide with the Cartesian coordinate planes, so the symmetry-plane orientation (Figure 1) is fixed throughout the model. The azimuths of the vertical symmetry planes of a horizontally layered orthorhombic medium can be estimated from the NMO ellipses or azimuthally varying amplitude-variation-with-offset (AVO) gradients of reflected waves (Grechka and Tsvankin, 1998; Vasconcelos and Tsvankin, 2006; Wang and Tsvankin, 2009; Tsvankin and Grechka, 2011). Here, we assume the orientation of the vertical symmetry planes to be known and spatially invariant.

There is a limited equivalence (that does not include geometric spreading) between the symmetry planes of orthorhombic media and any plane of transversely isotropic (TI) models that contains the symmetry axis (Tsvankin, 1997). This equivalence has been used in nonhyperbolic moveout analysis to build initial orthorhombic models by performing 2D VTI inversion in the vicinity of the symmetry planes (Vasconcelos and Tsvankin, 2006; Tsvankin and Grechka, 2011).

Likewise, here we apply 2D FWI for VTI media to the data in the vertical symmetry planes to estimate the in-plane VTI parameters. It should be noted that lateral heterogeneity and the difference between the geometric spreading in the symmetry planes of orthorhombic and VTI media could cause errors in the inversion results. Still, our approach produces a more accurate, higher-resolution initial model for orthorhombic FWI than that based solely on moveout inversion.

The 2D inversion, carried out in the vertical symmetry planes that cross the center of the model, yields the initial values of the parameters $\epsilon^{(1)}$, $\delta^{(1)}$, and $\gamma^{(1)}$ (for the $[x_2, x_3]$-plane) and $\epsilon^{(2)}$, $\delta^{(2)}$, and $\gamma^{(2)}$ (for the $[x_1, x_3]$-plane). The parameters V_{P0}, V_{S0}, and ρ are obtained in both symmetry planes. The parameter $\delta^{(3)}$ defined in the $[x_1, x_2]$-plane can be estimated by inverting the P-wave nonhyperbolic moveout or NMO ellipses from dipping reflectors (Tsvankin and Grechka, 2011). Here, we assume that the initial distribution of $\delta^{(3)}$ coincides with that of the parameter $\delta^{(2)}$.

The initial models for the VTI inversion in the symmetry planes (Figure 3) are obtained by applying 2D Gaussian smoothing of the actual parameters. The standard deviation (SD) of the smoothing kernel from the actual parameter distributions is set to 15. Similar long-wavelength initial models could be produced by 2D reflection tomography or moveout inversion (Vasconcelos and Tsvankin, 2006; Wang and Tsvankin, 2009, 2013a, 2013b). To build the initial 3D orthorhombic model, we extrapolate the values estimated by the 2D symmetry-plane inversion along an image of the inversion gradient (Hale, 2010). This image provides the orientation of the layer boundaries which are used to extrapolate the medium parameters. It is also possible to use prestack migrated sections generated using the energy-norm (Rocha et al., 2017) or other imaging conditions for elastic media (Duan and Sava, 2015).

Because the model is laterally heterogeneous, out-of-planes events could degrade the 2D symmetry-plane inversion results. Therefore, Gaussian smoothing (SD = 20 m) is applied to the estimated VTI parameters to suppress such artifacts. The initial orthorhombic model is smoothed again (SD = 40 m) before FWI to reduce the influence of artifacts on the employed gradient image.

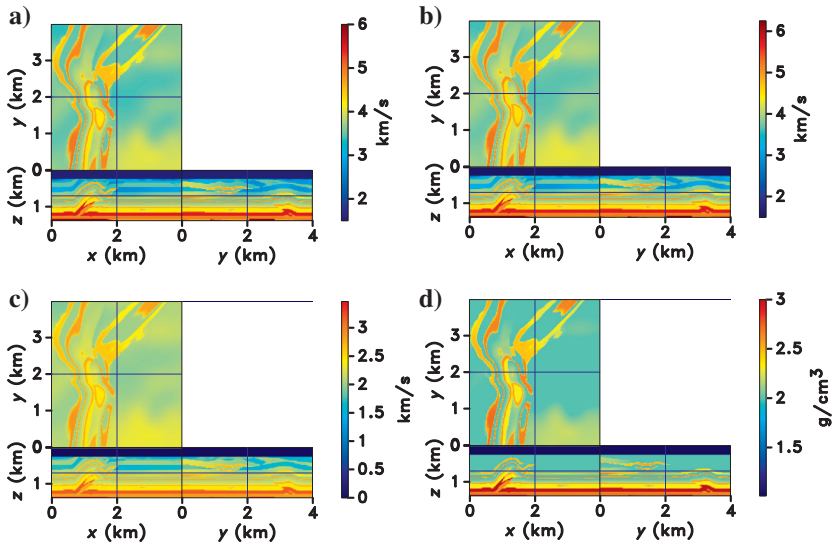

Figure 2. Parameters of an orthorhombic overthrust model: (a) the P-wave vertical velocity (V_{P0}), (b) the P-wave normal-moveout velocity in the $[x_2, x_3]$-plane ($V_{nmo,1}$), (c) the S-wave vertical velocity (V_{S0}), and (d) the density (ρ). The cross-sections display the parameters in the coordinate (symmetry) planes at the center of the model. The velocities not shown here have a spatial distribution similar to that of V_{P0}.

3D FWI for overthrust model

The initial parameter fields built using the above approach are employed to carry out full 3D elastic inversion for the orthorhombic overthrust model. The lower frequencies in the range 0–2 Hz, which are seldom available in the field, are removed by applying a bandpass Wiener filter to keep frequencies only between 2 and 19 Hz. As in most existing FWI algorithms, the inversion nonlinearity is partially mitigated using the multiscale approach (Bunks et al.,

1995) with four frequency bands (2–5 Hz, 2–8 Hz, 2–13 Hz, and 2–19 Hz). To suppress numerical artifacts, Gaussian-based smoothing (SD = 40 m) is applied to the inversion gradients (Modrak and Tromp, 2016).

To improve the convergence of the optimization method and avoid local minima of the objective function, the amplitude decay with depth due to geometric spreading and multiple reflections in the overburden needs to be compensated for. Hence, we precondition the inversion gradients using an approximation for the diagonal elements of the inverse of the Hessian matrix. The approximated Hessian is obtained by the zero-lag correlation of the magnitude of the forward wavefield with an approximate receiver Green's function (Plessix and Mulder, 2004). This procedure is implemented before the determination of the descent direction in the conjugate-gradient method. Hence, the direction of the parameter updating always follows the negative slope of the smoothed gradient.

The output of FWI without constraints (using $\beta = 0$ in equation 1) is shown in Figures 4 and 5. As explained below, the results are in general agreement with the study of the scattering (radiation) patterns for orthorhombic media (Singh and Tsvankin, 2020).

The P-wave horizontal velocities V_{P1} and V_{P2} are well resolved throughout the entire section, which is predicted by the radiation-pattern analysis. Although the P-wave vertical velocity V_{P0} is accurately estimated in the upper part of the section, the structural complexity of the V_{P0}-field is not fully reconstructed at depth. Despite the relatively weak sensitivity of FWI to the NMO velocities $V_{nmo,1}$ and $V_{nmo,2}$, they are estimated with acceptable accuracy in the upper part of the section (above 0.8 km) because the simulated data include intensive pure P-wave reflections (Singh and Tsvankin,

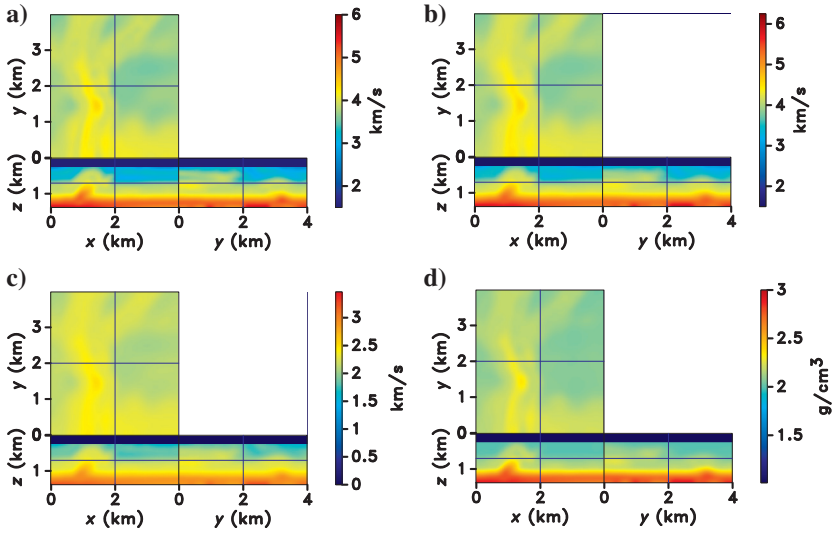

Figure 3. Initial parameters for the model in Figure 2: (a) V_{P0}, (b) $V_{nmo,1}$, (c) V_{S0}, and (d) ρ.

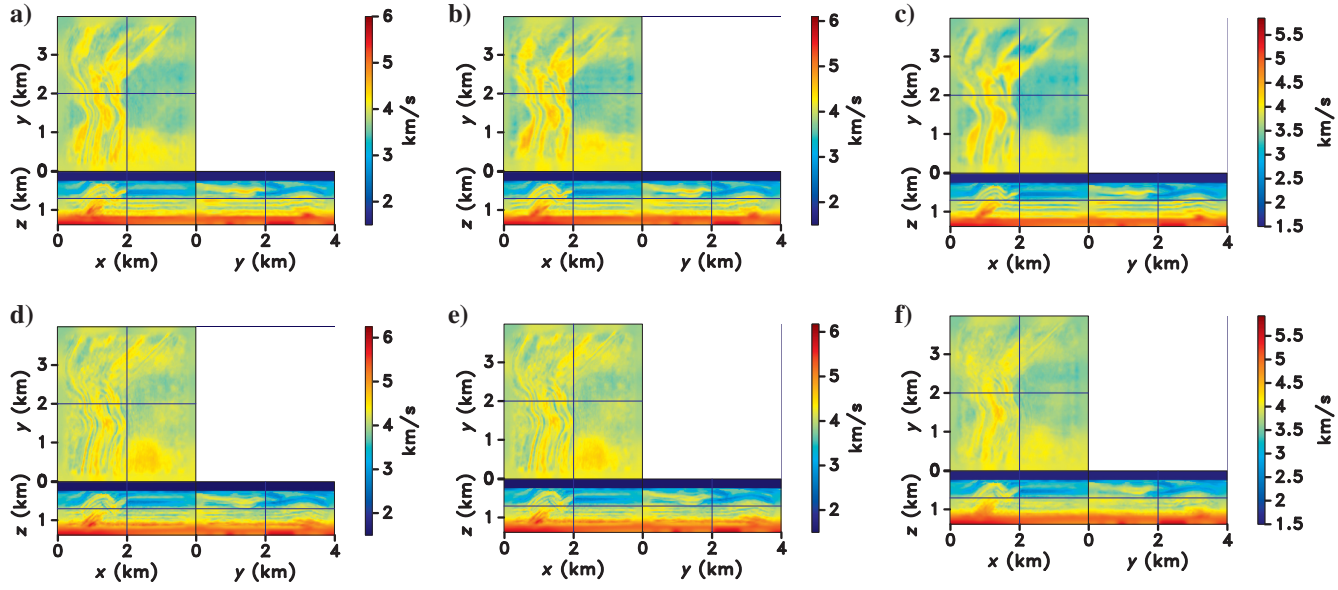

Figure 4. Results of the unconstrained FWI: (a) V_{P1}, (b) V_{P2}, (c) V_{P0}, (d) $V_{nmo,1}$, (e) $V_{nmo,2}$, and (f) $V_{nmo,3}$.

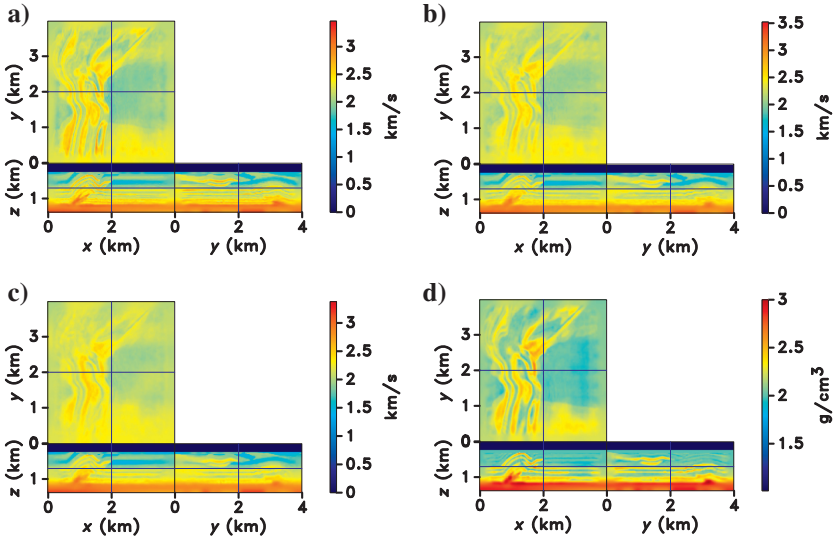

Figure 5. Results of the unconstrained FWI: (a) V_{S0}, (b) V_{S1}, (c) V_{S2}, and (d) ρ.

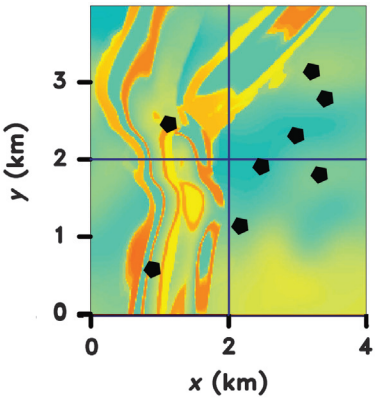

Figure 6. Depth slice of the velocity V_{P1} at $z = 0.7$ km. The locations of the well logs used for facies classification and image-guided interpolation are marked by the black polygons.

Table 1. Statistical parameter distributions for the training data set.

	V_{P0} (m/s)	V_{S0} (m/s)	ρ (g/cm^3)	Facies	Depth (m)
Mean	3624	1944	2.07	1.88	690
Std	1222	985	5.79	0.80	404
Min	1500	0	1.01	1.00	340
25%	2924	1688	2.00	1.00	340
50%	3646	2105	2.00	2.00	690
75%	4476	2584	2.44	3.00	1040
Max	6000	3464	3.00	3.00	1380

2020). As the velocity $V_{nmo,3}$ barely influences the objective function, it is the least resolved medium parameter, although it could be better constrained by longer-offset data.

Singh and Tsvankin (2020) show that a perturbation of the S-wave horizontal velocity V_{S2} scatters most of the energy close to the horizontal plane, so V_{S2} can be constrained only in the shallow part of the section. In contrast, the perturbations in the shear-wave vertical velocities (V_{S0} and V_{S1}) scatter energy towards the surface, and FWI succeeds in reconstructing the high-resolution fields of both parameters. The radiation patterns also suggest that there are trade-offs between V_{S0}, V_{S1}, and the P-wave NMO velocities $V_{nmo,1}$ and $V_{nmo,2}$. However, the scattering amplitudes for V_{S0} and V_{S1} are much larger than those for $V_{nmo,1}$ and $V_{nmo,2}$. Therefore, errors in the S-wave vertical velocities degrade the updates of the NMO velocities, but less so the other way around. Although the density is estimated with acceptable accuracy for most of the section, its values up shallow are distorted by the parameter trade-offs.

Next, we add facies information with the goal of mitigating the above parameter-estimation problems and improving the inversion results. To build a prior facies model from borehole data, we develop a novel approach based on machine learning.

MACHINE-LEARNING-BASED REGULARIZATION

Classification of lithologic facies involves estimation of rock lithology by analyzing such measurements as sonic and density well logs. Usually this classification is done manually by an experienced interpreter, which makes this process subjective and inefficient. Here we employ machine learning (ML), which is rapidly becoming a common tool in applied geophysics due to the advent of computing technology and availability of open-source ML libraries.

Our methodology for generating facies models via supervised machine learning is based on so-called Support Vector Machines (SVM). To classify facies for the entire model space, we follow the approach suggested by Hall (2016). However, the input data in our algorithm are derived from the elastic properties rather than the reservoir parameters, which allows the ML model to identify the underlying relations between the FWI-updated parameters and borehole data. SVM is a supervised-learning method that needs to be supplied with training data to build the relationships between the input features (in our case, elastic parameters) and the classes to which these features belong.

Our model includes eight randomly placed "boreholes" where sonic and density logs, as well as information about lithologic facies, are assumed to be available (Figure 6). The algorithm operates with three facies, which can be revealed by cross-plotting the P-wave vertical impedance (ρV_{P0}) and the S-wave vertical velocity V_{S0}. Therefore, only the parameters V_{P0}, V_{S0}, and ρ, which can be obtained from standard sonic and density logs, are employed for constructing the spatial facies model. The interpreted facies

are also assumed to be available at the borehole locations.

Thus, the input data for training the SVM model are the parameters V_{P0}, V_{S0}, ρ, and depth, which form a 4D space. The output is the facies interpreted at the boreholes; one of the boreholes is set aside for a blind test. In machine-learning terminology, the set of measurements at each depth interval forms a "feature vector" associated with a certain class (the facies type). An overview of the statistical distribution of the training data can be found in Table 1. Many machine-learning algorithms assume the feature data to be normally distributed (i.e., the distribution is Gaussian with zero mean and unit variance), which is not the case with our training data set (Table 1). Therefore, we condition (or standardize) the training data so that they acquire this property. The same parameters used to standardize the training data must be applied to any subsequently classified data set. The python-based "Scikit-learn" utility is employed to standardize the input data.

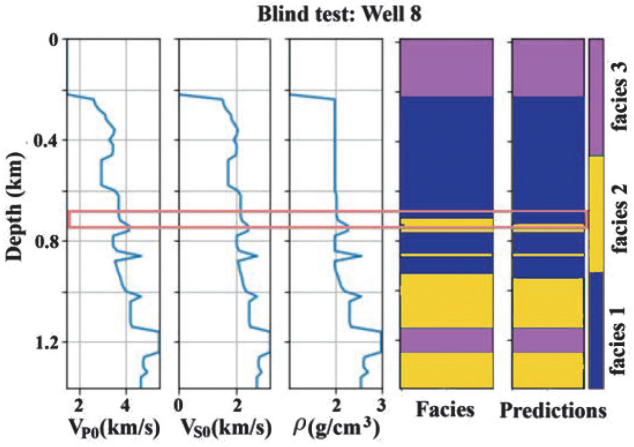

Figure 7. Facies classification for the "blind" well. The rectangle near 0.7 km marks a false facies prediction by the classification algorithm.

A common practice in training supervised-learning algorithms is to separate some data from the training set to evaluate the accuracy of the classifier. For that purpose, we employ the data from one of the wells. It is also helpful to have a cross-validation data set to tune the parameters of the ML network. We use 5% of the data for such cross-validation.

After splitting the input data, we use the conditioned data set to train a Support Vector Machine in facies classification. If the data were linearly separable, it would be easy to draw boundaries between the input data points and identify distinct classes. Otherwise, the data have to be projected into a higher-dimensional space for separation purposes. The boundaries for data separation are generated during the SVM training step implemented by employing a Gaussian-radial-basis kernel function.

During the training, the SVM algorithm achieves the accuracy close to 98% (or the 0.98 probability of predicting the correct facies), which is consistent with the testing on the blind well where the accuracy is 97% (Figure 7). Of course, such high accuracy can be expected in synthetic tests. However, efficient inclusion of ML models into the FWI framework should remain advantageous for field data, even though the errors are likely to increase.

For the first frequency band (2–8 Hz) of the constrained inversion, the facies distribution for the entire volume is built by the trained SVM that classifies the facies for the inverted model obtained by the unconstrained FWI for 2–5 Hz (Figure 8a). The facies models for the subsequent inversion stages (Figures 8b and 8c) are generated by the SVM classifier applied to the model obtained from the previous inversion stage of the facies-based FWI. This facies model allows us to predict the elastic properties, which could be incorporated into a regularization term in the objective function or used to build a better initial model for the next inversion stage. Below we discuss two implementations of regularization in the facies-based FWI algorithm.

Regularization (I)

This procedure employs the model obtained from the facies distribution as the starting model for the next inversion stage. The

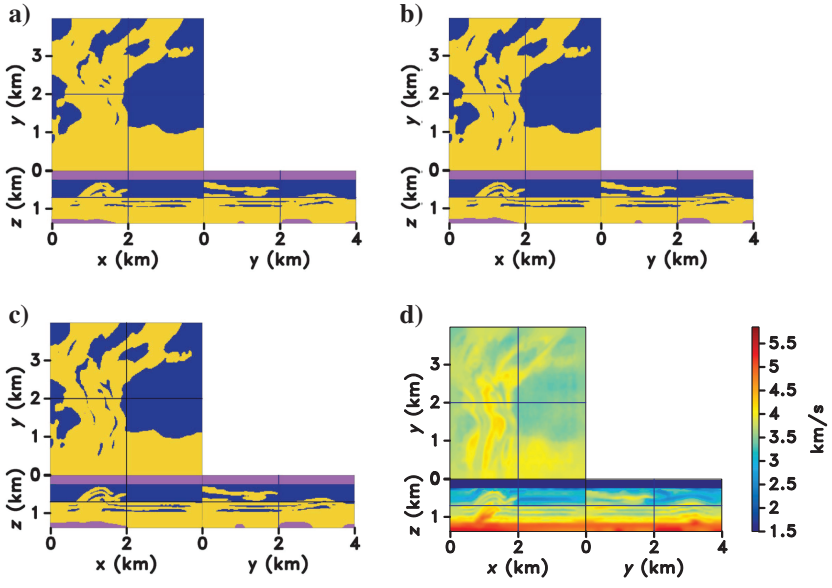

Figure 8. Automated facies generation (blue—facies 1; yellow—facies 2; pink—facies 3) for different frequency bands: (a) 2–5 Hz, (b) 2–8 Hz, and (c) 2–13 Hz. (d) The initial velocity V_{P0} for the orthorhombic model computed by the best-matching technique described in the main text.

model ($\mathbf{m}_{\text{inv}}$) is built by assigning at each grid point the best-matched elastic property between the inverted model and borehole data for a given facies:

$$\mathbf{m}_{\text{inv}}(i,j) = \mathbf{D}_T(n_{\min})|_{\text{facies(i,j)}}, \tag{12}$$

where

$$n_{\min} = \text{argmin}_{n=1:k}\{\mathbf{m}(i,j) - \mathbf{D}_T(n)|_{\text{facies(i,j)}}\}.$$

In equation 12, $\mathbf{m}$ is the current model, $\mathbf{D}_T$ is the data obtained from the boreholes, (i, j) indicate the spatial location in the staggered grid, and k is total number of the parameter values in $\mathbf{D}_T$ that correspond to a certain facies. After the elastic properties have been assigned, Gaussian-based smoothing (SD = 20 m) yields the initial model for FWI (Figure 8d). Note that the model $\mathbf{m}_{\text{inv}}$ obtained from equation 12 is used as the initial model for the next inversion stage and is substituted into equation 1. For later iterations, $\mathbf{m}_{\text{inv}}$ coincides with the inverted model $\mathbf{m}$. This procedure is repeated for the next inversion stage.

Since the SVM classification here is about 97% accurate, equation 12 is used to compute $\mathbf{m}_{\text{inv}}$ for all probable facies at each grid point. Because SVM algorithms do not directly provide probability estimates, the SVM "Scores and Probabilities" approach from "Scikit-learn" is used to compute the facies probabilities at each grid point (Wu et al., 2004). Hence, $\mathbf{m}_{\text{inv}}$ is constructed using a weighted summation of an elastic property for each probable facies [e.g., $\sum p(\text{facies}) * \mathbf{m}(i,j)$; p is the probability of the facies and $\mathbf{m}$ is the desired elastic property]. Whereas for the 2–5 Hz frequency range the unconstrained algorithm reduces the objective function by approximately 98%, the reduction of the objective function for the higher frequency band (2–8 Hz) is just 81%. Therefore, we obtain the initial model for the facies-based inversion using the results for the 2–5 Hz frequency range.

Regularization (II)

In addition to the facies-based constraints, the workflow incorporates direct information from sonic and density logs. Generally, well logs can be used to estimate the profiles of the vertical velocities V_{P0}, V_{S0}, V_{S1} (if dipole sonic logs are available), and density ρ. However, the anisotropy coefficients $\epsilon^{(1)}$, $\epsilon^{(2)}$, $\delta^{(1)}$, $\delta^{(2)}$, $\delta^{(3)}$, $\gamma^{(1)}$, and $\gamma^{(2)}$ (and, therefore, the corresponding velocities) are not constrained by well-log data. (Note that the difference $\gamma^{(1)} - \gamma^{(2)}$ can be obtained from dipole sonic logs.) Still, these coefficients potentially could be found from core measurements, as demonstrated by physical-modeling studies (Grechka et al., 1999). It is also possible to employ machine-learning algorithms to estimate some unavailable parameters (Singh and Kanli, 2016).

In our synthetic experiment, however, we assume that prior information is available only for V_{P0}, V_{S0}, and ρ. If any of the anisotropy coefficients can be measured on rock samples, the corresponding velocities (after an appropriate upscaling) can be incorporated into the ML framework to provide additional facies indicators and fine-tune the classification process.

Therefore, the term $\mathbf{m}_{\text{prior}}$ in the objective function (equation 1) incorporates the parameters V_{P0}, V_{S0}, and ρ estimated at the borehole locations and interpolated and extrapolated using a migrated image (Figure 9). As mentioned above, $\mathbf{W}_{\text{m}}$ is a weighting matrix designed to assign larger weights around the borehole locations, where accurate lithologic information is available. Furthermore, to be consistent with the gradient preconditioning applied to the

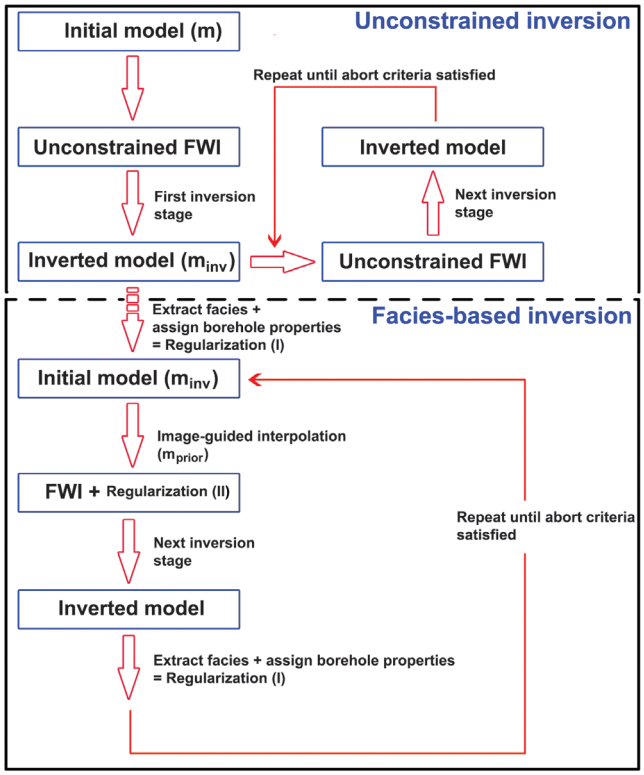

Figure 10. Workflow for the unconstrained and facies-based FWI.

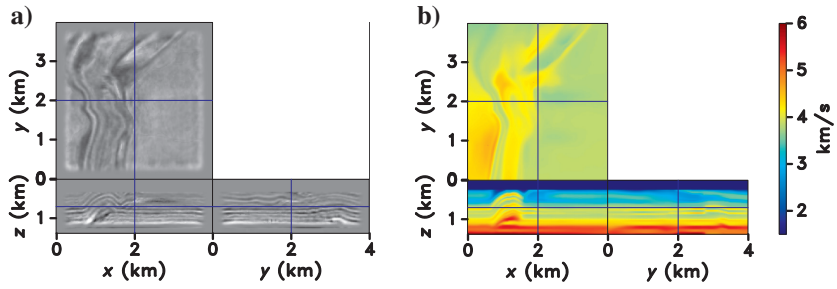

Figure 9. Image-guided interpolation used for regularizing the inversion. (a) The image of the inversion gradient and (b) the V_{P0}-field obtained by interpolating the well logs in Figure 6 using the image on plot (a).

data-fitting term (the first term in equation 10), we apply a correction for geometric spreading to the objective function (the second term in equation 10). This approach is similar to that in Singh et al. (2020b), where the operator $\mathbf{W}_m^T\mathbf{W}_m$ is scaled by $1/z^2$, where z is the depth. (Note that the amplitude decay due to geometric spreading approximately is inversely proportional to z.)

The improved facies-based initial models ($\mathbf{m}_{inv}$) and direct observation constraints ($\mathbf{m}_{prior}$) are the essential elements of our regularized FWI algorithm, whose results are discussed in the next section. The workflow of the entire algorithm that includes both the unconstrained and facies-based FWI is shown in Figure 10.

Application to overthrust model

As before, FWI is carried out for all three displacement components in the same four frequency bands (2–5 Hz, 2–8 Hz, 2–13 Hz, 2–19 Hz). This time, however, we use a more accurate facies-based initial model for each inversion stage. Additionally, the objective function includes the regularization term (equation 1) constructed from borehole data.

The addition of the facies information increases the accuracy of the inverted parameters (Figures 11 and 12). In particular, the vertical velocities V_{P0} and V_{S0} are estimated with a higher resolution for the entire depth range (Figure 13). Also, the constrained inver-

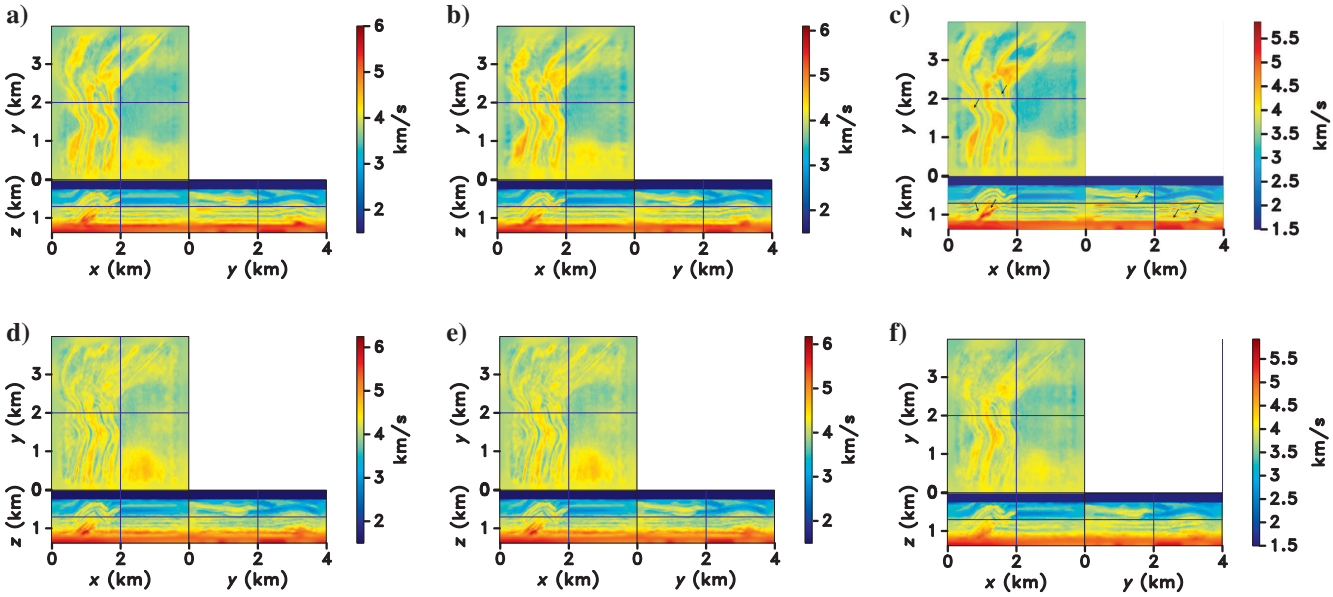

Figure 11. Results of the facies-based FWI: (a) V_{P1}, (b) V_{P2}, (c) V_{P0}, (d) $V_{nmo,1}$, (e) $V_{nmo,2}$, and (f) $V_{nmo,3}$. The arrows on plot (c) mark regions of increased spatial resolution and accuracy.

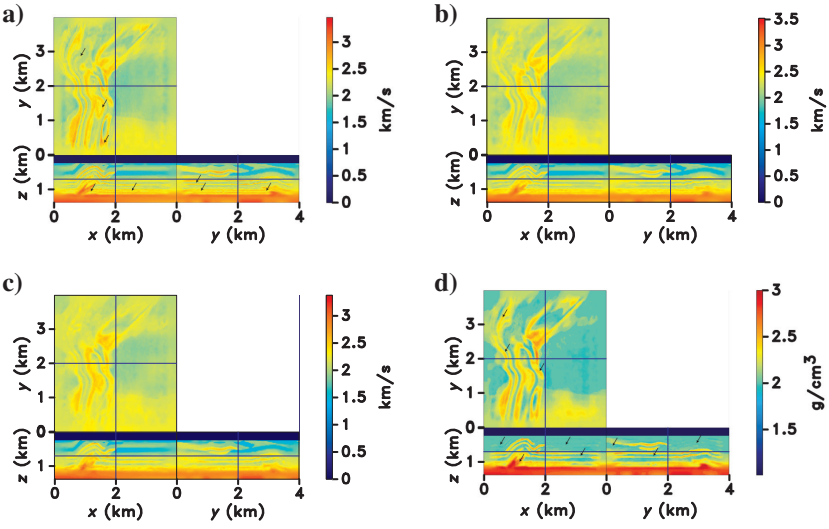

Figure 12. Results of the facies-based FWI: (a) V_{S0}, (b) V_{S1}, (c) V_{S2}, and (d) ρ. The arrows on plots (a) and (d) mark regions of increased spatial resolution and accuracy.

DOI:10.1190/geo2020-0512.1

sion substantially reduces the distortions in the shallow part of the density field (compare Figure 12d to the output of the unconstrained FWI in Figure 5d). The improvements in the inverted P-wave NMO velocities $V_{\mathrm{nmo},1}$ and $V_{\mathrm{nmo},2}$, however, are relatively small (compare Figures 11d and 11e to Figures 4d and 4e) because of the weaker sensitivity of FWI to these parameters (see above). The velocity updates displayed in Figure 14 further illustrate the higher effectiveness of the facies-based inversion compared to the unconstrained FWI. Although the velocity $V_{\mathrm{nmo},3}$ is estimated with a somewhat higher accuracy due to the improved recovery of the other parameters, it remains poorly resolved for most of the model.

It is also instructive to compare seismograms computed for the models obtained by the unconstrained and facies-based inversion (Figure 15). The wavefield for the model reconstructed by our facies-based algorithm provides a better fit to the observed data.

To generate the final spatial distribution of the facies, the trained and tested SVM is supplied with the inverted vertical velocities V_{P0} and V_{S0} and density (Figure 16). This facies model that incorporates the FWI results provides high-resolution information for reservoir characterization. Although here we present a simplified model consisting of three facies, the proposed scheme can be extended to more

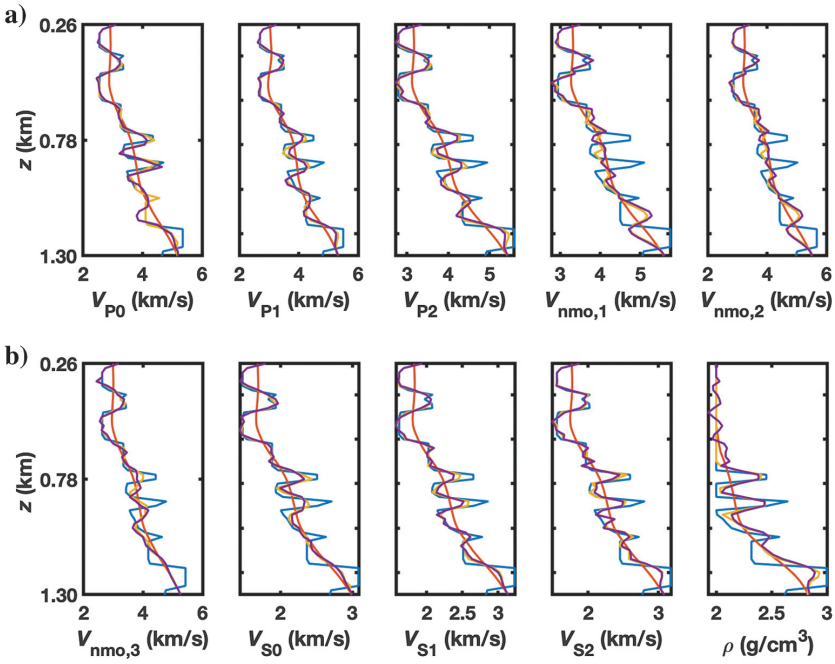

Figure 13. Vertical parameter profiles at $x = y = 110$ km. The actual and initial parameters are marked by the blue and red lines, respectively. The parameters estimated by the unconstrained and facies-based FWI are marked by the violet and yellow lines, respectively.

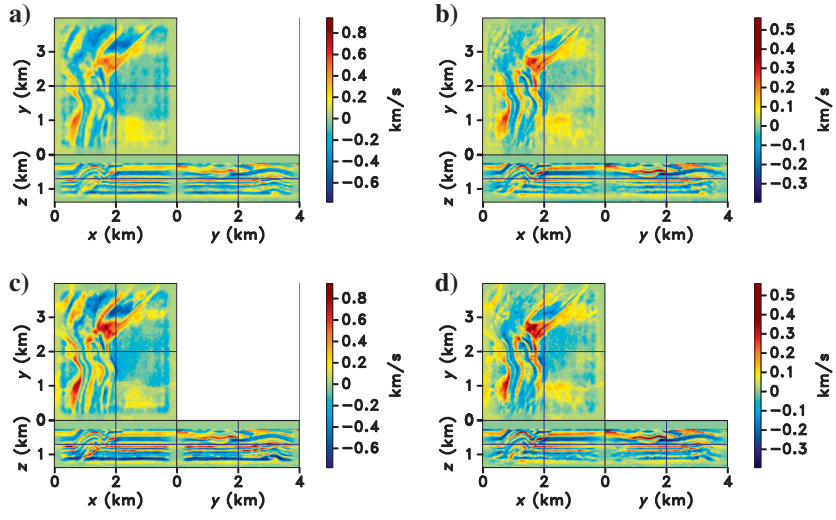

Figure 14. Difference between the parameters (a) V_{P0} and (b) V_{S0} estimated by the unconstrained FWI and their initial values. The difference between the parameters (c) V_{P0} and (d) V_{S0} estimated by the facies-based FWI and their initial values.

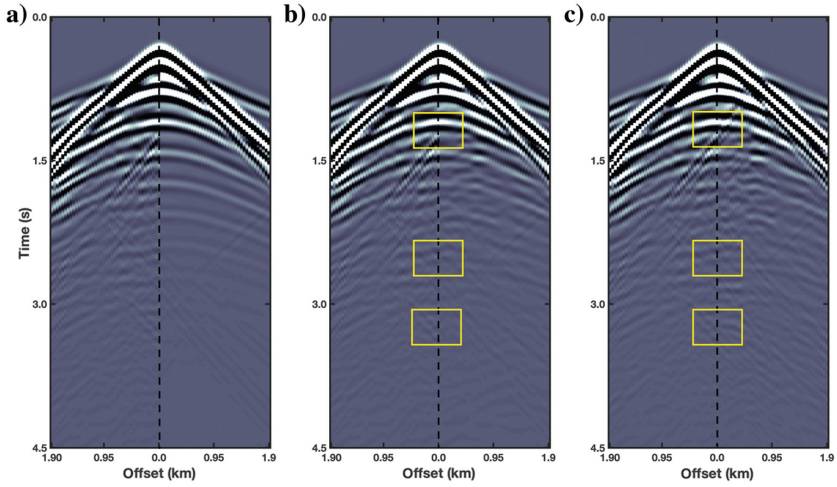

Figure 15. Vertical displacement from shot #50 at $x = y = 2$ km. The panel to left of the dashed line contains the seismogram for the actual model, and to the right are the seismograms for the (a) initial model, (b) model from the unconstrained inversion, and (c) model from the facies-based inversion. The yellow boxes on plots (b) and (c) mark regions where the two wavefields differ from one another.

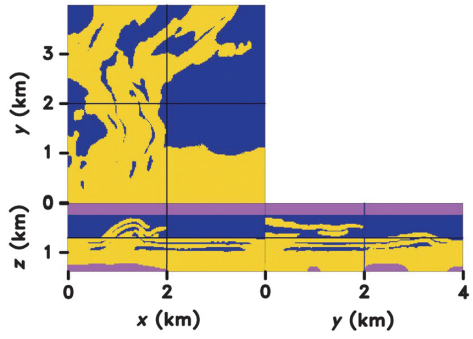

Figure 16. Facies model built automatically using the inverted parameters from Figures 11 and 12.

facies, as long as they are supported by prior knowledge of the study area.

CONCLUSIONS

We have developed an efficient framework for extending 3D elastic full-waveform inversion to orthorhombic models, which are needed to properly describe many subsurface formations. The algorithm uses a velocity-based parameterization that is particularly effective in resolving the P- and S-wave symmetry-direction velocities. The P-wave normal-moveout velocities, however, are more difficult to estimate because their influence on the objective function is relatively weak. A detailed analysis of the sensitivity of FWI to the parameters of orthorhombic media is presented in another article.

To mitigate the trade-offs between multiple parameters of orthorhombic media, our algorithm incorporates prior information about the available geologic facies. To address the sparsity of well logs, which are used to identify the facies, a supervised machine-learning technique (Support Vector Machine or SVM) is employed to build a 3D facies distribution. Once that distribution for a given inversion stage has been obtained, the elastic properties for each probable facies at all grid points are computed by matching the model obtained at the previous stage to the borehole data. This process yields the parameter fields that form the initial model for that inversion stage. Additional lithologic constraints are incorporated directly into the objective function using image-guided interpolation of the borehole (well-log) data with larger weights assigned to the vicinity of the borehole locations.

Application of this algorithm to a 3D orthorhombic overthrust model results in a substantial improvement in the spatial resolution of most inverted parameters compared to the output of the unconstrained FWI. [It should be noted that the performance of the unconstrained FWI is in broad agreement with the analysis of the radiation (scattering) patterns.] In particular, the P- and S-wave velocities in the symmetry directions (especially the vertical velocities) are estimated with much higher accuracy, even without ultra-low-frequency (0–2 Hz) data. The algorithm also produces a better density model for the shallow part of the model. There is an improvement in the inverted P-wave NMO velocities as well, although the velocity $V_{\mathrm{nmo},3}$ remains the least-resolved medium parameter.

ACKNOWLEDGMENTS

This work was supported by the Consortium Project on Seismic Inverse Methods for Complex Structures at the Center for Wave Phenomena (CWP). We thank Vladimir Li from Ikon Science, UK for his help with 3D image-guided interpolation. We are grateful to the members of the A(anisotropy)-Team at CWP for useful discussions.

DATA AND MATERIALS AVAILABILITY

Data associated with this research are available and can be obtained by contacting the corresponding author.

APPENDIX A

INVERSION GRADIENTS FOR ORTHORHOMBIC MEDIA

We assume that the symmetry planes of orthorhombic media coincide with the coordinate planes of a Cartesian coordinate frame. The model is parameterized by the P- and S-wave vertical velocities (V_{P0}, V_{S0}, and V_{S1}), P- and S-wave symmetry-direction horizontal velocities (V_{P1}, V_{P2}, and V_{S2}), P-wave normal-moveout velocities ($V_{\mathrm{nmo},1}$, $V_{\mathrm{nmo},2}$, and $V_{\mathrm{nmo},3}$), and density (ρ) (see equations 3–9). The pertinent stiffness coefficients in the two-index (Voigt) notation are related to these velocities as follows:

DOI:10.1190/geo2020-0512.1

$$c_{11} = \rho V_{P2}^2, \tag{A-1}$$

$$c_{22} = \rho V_{P1}^2, \tag{A-2}$$

$$c_{33} = \rho V_{P0}^2, \tag{A-3}$$

$$c_{12} = \rho\left\{\sqrt{[V_{P2}^2 - V_{S2}^2][V_{nmo,3}^2 - V_{S2}^2]} - V_{S2}^2\right\}, \tag{A-4}$$

$$c_{13} = \rho\left\{\sqrt{[V_{P0}^2 - V_{S0}^2][V_{nmo,2}^2 - V_{S0}^2]} - V_{S0}^2\right\}, \tag{A-5}$$

$$c_{23} = \rho\left\{\sqrt{[V_{P0}^2 - V_{S1}^2][V_{nmo,1}^2 - V_{S1}^2]} - V_{S1}^2\right\}, \tag{A-6}$$

$$c_{44} = \rho V_{S1}^2, \tag{A-7}$$

$$c_{55} = \rho V_{S0}^2, \tag{A-8}$$

$$c_{66} = \rho V_{S2}^2. \tag{A-9}$$

The gradient of the l^2-norm objective function (equation 1; $\beta = 0$) for arbitrarily anisotropic elastic media is obtained by Kamath and Tsvankin (2016) as:

$$\frac{\partial E}{\partial m_n} = -\sum_{ijkl} \frac{\partial c_{ijkl}}{\partial m_n}\left(\int_0^T \frac{\partial u_i}{\partial x_j}\frac{\partial \psi_k}{\partial x_l}\right), \tag{A-10}$$

where the indices $i, j, k, l = 1, 2, 3$, T is the total time of wave propagation, $\mathbf{u}$ and $\boldsymbol{\psi}$ are the forward- and back-propagated displacement fields, respectively, and the vector $\mathbf{m}$ includes the model parameters (in our case, $m_1 = V_{P0}$, $m_2 = V_{P1}$, $m_3 = V_{P2}$, $m_4 = V_{nmo,1}$, $m_5 = V_{nmo,2}$, $m_6 = V_{nmo,3}$, $m_7 = V_{S0}$, $m_8 = V_{S1}$, $m_9 = V_{S2}$, and $m_{10} = \rho$).

The derivatives of the objective function with respect to these parameters are (here $x = x_1$, $y = x_2$, and $z = x_3$):

$$\frac{\partial E}{\partial V_{P0}} = -2\rho V_{P0}\int_0^T \left[\left(\frac{\partial \psi_z}{\partial z}\frac{\partial u_x}{\partial x} + \frac{\partial \psi_x}{\partial x}\frac{\partial u_z}{\partial z}\right)\frac{q_2}{2} + \left(\frac{\partial \psi_y}{\partial y}\frac{\partial u_z}{\partial z} + \frac{\partial \psi_z}{\partial z}\frac{\partial u_y}{\partial y}\right)\frac{q_3}{2} + \frac{\partial \psi_z}{\partial z}\frac{\partial u_z}{\partial z}\right]dt, \tag{A-11}$$

$$\frac{\partial E}{\partial V_{P1}} = -2\rho V_{P1}\int_0^T \left(\frac{\partial \psi_y}{\partial y}\frac{\partial u_y}{\partial y}\right)dt, \tag{A-12}$$

$$\frac{\partial E}{\partial V_{P2}} = -2\rho V_{P2}\int_0^T \left[\left(\frac{\partial \psi_x}{\partial x}\frac{\partial u_y}{\partial y} + \frac{\partial \psi_y}{\partial y}\frac{\partial u_x}{\partial x}\right)\frac{q_1}{2} + \frac{\partial \psi_x}{\partial x}\frac{\partial u_x}{\partial x}\right]dt, \tag{A-13}$$

$$\frac{\partial E}{\partial V_{nmo,1}} = -\rho V_{nmo,1}\int_0^T \left[\left(\frac{\partial \psi_y}{\partial y}\frac{\partial u_z}{\partial z} + \frac{\partial \psi_z}{\partial z}\frac{\partial u_y}{\partial y}\right)\frac{1}{q_3}\right]dt, \tag{A-14}$$

$$\frac{\partial E}{\partial V_{nmo,2}} = -\rho V_{nmo,2}\int_0^T \left[\left(\frac{\partial \psi_z}{\partial z}\frac{\partial u_x}{\partial x} + \frac{\partial \psi_x}{\partial x}\frac{\partial u_z}{\partial z}\right)\frac{1}{q_2}\right]dt, \tag{A-15}$$

$$\frac{\partial E}{\partial V_{nmo,3}} = -\rho V_{nmo,3}\int_0^T \left[\left(\frac{\partial \psi_y}{\partial y}\frac{\partial u_x}{\partial x} + \frac{\partial \psi_x}{\partial x}\frac{\partial u_y}{\partial y}\right)\frac{1}{q_1}\right]dt, \tag{A-16}$$

$$\frac{\partial E}{\partial V_{S0}} = -\rho V_{S0}\int_0^T \left[\left(\frac{\partial \psi_z}{\partial z}\frac{\partial u_x}{\partial x} + \frac{\partial \psi_x}{\partial x}\frac{\partial u_z}{\partial z}\right)\left(-q_2 - \frac{1}{q_2} - 2\right) + 2\left(\frac{\partial \psi_x}{\partial z} + \frac{\partial \psi_z}{\partial x}\right)\left(\frac{\partial u_x}{\partial z} + \frac{\partial u_z}{\partial x}\right)\right]dt, \tag{A-17}$$

$$\frac{\partial E}{\partial V_{S1}} = -\rho V_{S1}\int_0^T \left[\left(\frac{\partial \psi_z}{\partial z}\frac{\partial u_y}{\partial y} + \frac{\partial \psi_y}{\partial y}\frac{\partial u_z}{\partial z}\right)\left(-q_3 - \frac{1}{q_3} - 2\right) + 2\left(\frac{\partial \psi_y}{\partial z} + \frac{\partial \psi_z}{\partial y}\right)\left(\frac{\partial u_y}{\partial z} + \frac{\partial u_z}{\partial y}\right)\right]dt, \tag{A-18}$$

$$\frac{\partial E}{\partial V_{S2}} = -\rho V_{S2}\int_0^T \left[\left(\frac{\partial \psi_y}{\partial y}\frac{\partial u_x}{\partial x} + \frac{\partial \psi_x}{\partial x}\frac{\partial u_y}{\partial y}\right)\left(-q_1 - \frac{1}{q_1} - 2\right) + 2\left(\frac{\partial \psi_x}{\partial y} + \frac{\partial \psi_y}{\partial x}\right)\left(\frac{\partial u_x}{\partial y} + \frac{\partial u_y}{\partial x}\right)\right]dt, \tag{A-19}$$

$$\begin{aligned}\frac{\partial E}{\partial \rho} = -\int_0^T \Bigg\{ & V_{P0}^2\left(\frac{\partial u_z}{\partial z}\frac{\partial \psi_z}{\partial z}\right) + V_{P1}^2\left(\frac{\partial u_y}{\partial y}\frac{\partial \psi_y}{\partial y}\right) + V_{P2}^2\left(\frac{\partial u_x}{\partial x}\frac{\partial \psi_x}{\partial x}\right) + \\ & \left[\sqrt{(V_{nmo,3}^2 - V_{S2}^2)(V_{P2}^2 - V_{S2}^2)} - V_{S2}^2\right]\left(\frac{\partial \psi_y}{\partial y}\frac{\partial u_x}{\partial x} + \frac{\partial \psi_x}{\partial x}\frac{\partial u_y}{\partial y}\right) + \\ & \left[\sqrt{(V_{nmo,2}^2 - V_{S0}^2)(V_{P0}^2 - V_{S0}^2)} - V_{S0}^2\right]\left(\frac{\partial \psi_z}{\partial z}\frac{\partial u_x}{\partial x} + \frac{\partial \psi_x}{\partial x}\frac{\partial u_z}{\partial z}\right) + \\ & \left[\sqrt{(V_{nmo,1}^2 - V_{S1}^2)(V_{P0}^2 - V_{S1}^2)} - V_{S1}^2\right]\left(\frac{\partial \psi_z}{\partial z}\frac{\partial u_y}{\partial y} + \frac{\partial \psi_y}{\partial y}\frac{\partial u_z}{\partial z}\right) + \\ & V_{S0}\left(\frac{\partial \psi_x}{\partial z} + \frac{\partial \psi_z}{\partial x}\right)\left(\frac{\partial u_x}{\partial z} + \frac{\partial u_z}{\partial x}\right) + V_{S1}^2\left(\frac{\partial \psi_z}{\partial y} + \frac{\partial \psi_y}{\partial z}\right)\left(\frac{\partial u_z}{\partial y} + \frac{\partial u_y}{\partial z}\right) + \\ & V_{S2}^2\left(\frac{\partial \psi_x}{\partial y} + \frac{\partial \psi_y}{\partial x}\right)\left(\frac{\partial u_y}{\partial x} + \frac{\partial u_x}{\partial y}\right) + v_x\Psi_x + v_y\Psi_y + v_z\Psi_z\Bigg\}\mathrm{d}t,\end{aligned} \tag{A-20}$$

where

$$q_1 = \sqrt{\frac{V_{\mathrm{nmo},3}^2 - V_{\mathrm{S2}}^2}{V_{\mathrm{P2}}^2 - V_{\mathrm{S2}}^2}}, \quad q_2 = \sqrt{\frac{V_{\mathrm{nmo},2}^2 - V_{\mathrm{S0}}^2}{V_{\mathrm{P0}}^2 - V_{\mathrm{S0}}^2}},$$

and

$$q_3 = \sqrt{\frac{V_{\mathrm{nmo},1}^2 - V_{\mathrm{S1}}^2}{V_{\mathrm{P0}}^2 - V_{\mathrm{S1}}^2}}.$$

Here $\mathbf{v}$ and $\boldsymbol{\Psi}$ are the forward- and back-propagated velocity fields, respectively.

REFERENCES

Alkhalifah, T., and R.-E. Plessix, 2014, A recipe for practical full-waveform inversion in anisotropic media: An analytical parameter resolution study: Geophysics, **79**, no. 3, R91–R101, doi: 10.1190/geo2013-0366.1.

Bakulin, A., V. Grechka, and I. Tsvankin, 2000, Estimation of fracture parameters from reflection seismic data — Part 2: Fractured models with orthorhombic symmetry: Geophysics, **65**, 1803–1817, doi: 10.1190/1.1444864.

Bohlen, T., 2002, Parallel 3-D viscoelastic finite-difference seismic modelling: Computers & Geosciences, **28**, 887–899, doi: 10.1016/S0098-3004(02)00006-7.

Bunks, C., F. M. Saleck, S. Zaleski, and G. Chavent, 1995, Multiscale seismic waveform inversion: Geophysics, **60**, 1457–1473, doi: 10.1190/1.1443880.

Duan, Y., and P. Sava, 2015, Scalar imaging condition for elastic reverse time migration: Geophysics, **80**, no. 4, S127–S136, doi: 10.1190/geo2014-0453.1.

Grechka, V., A. Pech, and I. Tsvankin, 2005, Parameter estimation in orthorhombic media using multicomponent wide-azimuth reflection data: Geophysics, **70**, no. 2, D1–D8, doi: 10.1190/1.1897026.

Grechka, V., S. Theophanis, and I. Tsvankin, 1999, Joint inversion of P- and PS-waves in orthorhombic media: Theory and a physical modeling study: Geophysics, **64**, 146–161, doi: 10.1190/1.1444512.

Grechka, V., and I. Tsvankin, 1998, 3-D description of normal moveout in anisotropic inhomogeneous media: Geophysics, **63**, 1079–1092, doi: 10.1190/1.1444386.

Hager, W. W., and H. Zhang, 2006, A survey of nonlinear conjugate gradient methods: Pacific Journal of Optimization, **6**, 35–58.

Hale, D., 2010, Image-guided 3D interpolation of borehole data: 80th Annual International Meeting, SEG, Expanded Abstracts, 1266–1270, doi: 10.1190/1.3513074.

Hall, B., 2016, Facies classification using machine learning: The Leading Edge, **35**, 906–909, doi: 10.1190/tle35100906.1.

Kamath, N., and I. Tsvankin, 2016, Elastic full-waveform inversion for VTI media: Methodology and sensitivity analysis: Geophysics, **81**, no. 2, C53–C68, doi: 10.1190/geo2014-0586.1.

Li, X.-Y., and J. Yuan, 1999, Converted-wave moveout and parameter estimation for transverse isotropy: 61st Annual International Conference and Exhibition, EAGE, Extended Abstracts, 1–4, doi: 10.3997/2214-4609.201407801.

Li, Y., W. Han, C.-S. Chen, and T. Huang, 2012, Velocity model building for tilted orthorhombic depth imaging: 82nd Annual International Meeting, SEG, Expanded Abstracts, doi: 10.1190/segam2012-1231.1.

Liu, Q., and J. Tromp, 2006, Finite frequency kernels based on adjoint methods: Bulletin of the Seismological Society of America, **96**, 2383–2397, doi: 10.1785/0120060041.

Liu, Q., and I. Tsvankin, 2019, Stacking-velocity tomography for tilted orthorhombic media: Geophysics, **84**, no. 3, C171–C180, doi: 10.1190/geo2018-0300.1.

Maitra, S., F. F. Basir, M. L. Ghazali, A. R. Ghazali, S. M. Sapiai, N. El-K, and T. Konuk, 2018, Orthorhombic full-waveform inversion and model building for azimuthal anisotropy in the presence of gas bodies: 88th Annual International Meeting, SEG, Expanded Abstracts, 5123–5127, doi: 10.1190/segam2018-2995810.1.

Masmoudi, N., and T. Alkhalifah, 2018, Full-waveform inversion in acoustic orthorhombic media and application to a North Sea data set: Geophysics, **83**, no. 5, C179–C193, doi: 10.1190/geo2017-0738.1.

Modrak, R., and J. Tromp, 2016, Seismic waveform inversion best practices: Regional, global and exploration test cases: Geophysical Journal International, **206**, 1864–1889, doi: 10.1093/gji/ggw202.

Oh, J.-W., and T. Alkhalifah, 2016, Elastic orthorhombic anisotropic parameter inversion: An analysis of parameterization: Geophysics, **81**, no. 6, C279–C293, doi: 10.1190/geo2015-0656.1.

Oh, J.-W., and T. Alkhalifah, 2019, Study on the full-waveform inversion strategy for 3D elastic orthorhombic anisotropic media: Application to ocean bottom cable data: Geophysical Prospecting, **67**, 1219–1242, doi: 10.1111/1365-2478.12768.

Plessix, R.-E., and W. A. Mulder, 2004, Frequency-domain finite-difference amplitude-preserving migration: Geophysical Journal International, **157**, 975–987, doi: 10.1111/j.1365-246X.2004.02282.x.

Rocha, D., N. Tanushev, and P. Sava, 2017, Anisotropic elastic wavefield imaging using the energy norm: Geophysics, **82**, no. 3, S225–S234, doi: 10.1190/geo2016-0424.1.

Rusmanugroho, H., R. Modrak, and J. Tromp, 2017, Anisotropic full-waveform inversion with tilt-angle recovery: Geophysics, **82**, no. 3, R135–R151, doi: 10.1190/geo2016-0025.1.

Singh, S., and A. I. Kanli, 2016, Estimating shear wave velocities in oil fields: A neural network approach: Geosciences Journal, **20**, 221–228, doi: 10.1007/s12303-015-0036-z.

Singh, S., and I. Tsvankin, 2020, Sensitivity analysis of FWI for elastic orthorhombic media: 90th Annual International Meeting, SEG, Expanded Abstracts, 171–175, doi: 10.1190/segam2020-3399390.1.

Singh, S., I. Tsvankin, and E. Zabihi Naeini, 2018, Bayesian framework for elastic full-waveform inversion with facies information: The Leading Edge, **37**, 924–931, doi: 10.1190/tle37120924.1.

Singh, S., I. Tsvankin, and E. Zabihi Naeini, 2019, Bayesian approach to facies-constrained waveform inversion for VTI media: 89th Annual International Meeting, SEG, Expanded Abstracts, 1370–1374, doi: 10.1190/segam2019-3214511.1.

Singh, S., I. Tsvankin, and E. Zabihi Naeini, 2020a, Elastic full-waveform inversion with geologic information for tilted TI media: 82nd Annual International Conference and Exhibition, EAGE, Extended Abstracts, 1–5, doi: 10.3997/2214-4609.202010224

Singh, S., I. Tsvankin, and E. Zabihi Naeini, 2020b, Full-waveform inversion for elastic VTI media with borehole constraints: Geophysics, **85**, no. 6, R553–R563, doi: 10.1190/geo2019-0816.1.

Tarantola, A., 1984, Inversion of seismic reflection data in the acoustic approximation: Geophysics, **49**, 1259–1266, doi: 10.1190/1.1441754.

Thomsen, L., 1986, Weak elastic anisotropy: Geophysics, **51**, 1954–1966, doi: 10.1190/1.1442051.

Tsvankin, I., 1997, Anisotropic parameters and P-wave velocity for orthorhombic media: Geophysics, **62**, 1292–1309, doi: 10.1190/1.1444231.

Tsvankin, I., 2012, Seismic signatures and analysis of reflection data in anisotropic media, 3rd ed.: SEG.

Tsvankin, I., and V. Grechka, 2011, Seismology of azimuthally anisotropic media and seismic fracture characterization: SEG.

Vasconcelos, I., and I. Tsvankin, 2006, Nonhyperbolic moveout inversion of wide azimuth P-wave data for orthorhombic media: Geophysical Prospecting, **54**, 535–552, doi: 10.1111/j.1365-2478.2006.00559.x.

Wang, H., and I. Tsvankin, 2018, Methodology of waveform inversion for acoustic orthorhombic media: Journal of Seismic Exploration, **27**, 201–226.

Wang, X., and I. Tsvankin, 2009, Estimation of interval anisotropy parameters using velocity-independent layer stripping: Geophysics, **74**, no. 5, WB117–WB127, doi: 10.1190/1.3157462.

Wang, X., and I. Tsvankin, 2013a, Multiparameter TTI tomography of P-wave reflection and VSP data: Geophysics, **78**, no. 5, WC51–WC63, doi: 10.1190/geo2012-0394.1.

Wang, X., and I. Tsvankin, 2013b, Ray-based gridded tomography for tilted transversely isotropic media: Geophysics, **78**, no. 1, C11–C23, doi: 10.1190/geo2012-0066.1.

Wu, T.-F., C.-J. Lin, and R. C. Wang, 2004, Probability estimates for multi-class classification by pairwise coupling: Journal of Machine Learning Research, **5**, 975–1005.

Xie, Y., B. Zhou, J. Zhou, J. Hu, L. Xu, X. Wu, N. Lin, F.-C. Loh, L. Liu, and Z. Wang, 2017, Orthorhombic full-waveform inversion for imaging the Luda field using wide-azimuth ocean-bottom-cable data: The Leading Edge, **36**, 75–80, doi: 10.1190/tle36010075.1.

Zhang, Z., and T. Alkhalifah, 2019, Regularized elastic full-waveform inversion using deep learning: Geophysics, **84**, no. 5, R741–R751, doi: 10.1190/geo2018-0685.1.

Zhang, Z., and T. Alkhalifah, 2020, High-resolution reservoir characterization using deep learning-aided elastic full-waveform inversion: The North Sea field data example: Geophysics, **85**, no. 4, WA137–WA146, doi: 10.1190/geo2019-0340.1.

Zhang, Z., T. Alkhalifah, E. Zabihi Naeini, and B. Sun, 2018, Multiparameter elastic full waveform inversion with facies-based constraints: Geophysical Journal International, **213**, 2112–2127, doi: 10.1093/gji/ggy113.

Sagar Singh received an Integrated Master of Technology degree (2016) in geophysical technology from the Indian Institute of Technology Roorkee. After graduation, he joined an IT firm where he worked on computer vision and machine learning. Before joining the Center for Wave Phenomena in the Fall of 2017, as a Ph.D. candidate, he worked in the fields of seismic imaging, inversion, and high-performance computing at NGRI (Hydrabad), KAUST (Saudi Arabia), and SNU (South Korea). He is currently working on anisotropic waveform inversion for reservoir characterization. His research interests include reservoir characterization, deep learning, and uncertainty analysis.

Ilya Tsvankin received an M.S. (1978) and Ph.D. (1982) in geophysics from Moscow State University in Russia. From 1978 to 1989, he worked at the Institute of Physics of the Earth in Moscow and was deputy head of laboratory "Geophysics of Anisotropic Media." After moving to the United States in 1990, he became a consultant to the Amoco Production Research Center in Tulsa. Since 1992, he has been on the faculty of Colorado School of Mines, where currently he is a professor of geophysics and director of the Center for Wave Phenomena. His research has focused on seismic modeling, inversion, and processing for anisotropic media, fracture characterization, time-lapse seismic, and nonlinear elasticity. For his work in seismic anisotropy, in 1996, he received the Virgil Kauffman Gold Medal Award from SEG. Among his other recognitions are the SEG Best Paper in Geophysics Award (2009), election to Fellowship of the Institute of Physics (2011), SEG Honorary Membership Award (2015), and SEG Outstanding Educator Award (2020). The third edition of his widely used monograph "Seismic signatures and analysis of reflection data in anisotropic media" was published by SEG in 2012. He also coauthored (with Vladimir Grechka) the book "Seismology of azimuthally anisotropic media and seismic fracture characterization" (SEG, 2011).

Ehsan Zabihi Naeini received a B.S. in physics, and an M.S. and a Ph.D. in geophysics. He has more than 15 years extensive software and technology development experience in geoscience software industry and has published numerous papers. His research interests include machine learning, data science, signal processing, physics driven subsurface analysis, and inversion.

DOI:10.1190/geo2020-0512.1